Advancements in Aerodynamic Shape Optimization with Hybrid Laminar Flow Control for Infinite Swept and Finite Wings at Cruise Conditions

Justin M. Pascual * and David W. Zingg [†]

Institute for Aerospace Studies, University of Toronto, ON M3H 5T6

Hybrid Laminar Flow Control (HLFC) enables the extension of laminar flow regions beyond the limitations of Natural Laminar Flow (NLF) by integrating passive shaping strategies with active boundary-layer suction. In this paper, a suction boundary condition is implemented within a Reynolds-averaged Navier–Stokes aerodynamic shape optimization framework coupled with the SA-sLM2015cc local correlation-based transition model. The methodology is applied to lift-constrained drag-minimization of two-dimensional airfoils, infinite swept wings, and finite wings at cruise conditions. Emphasis is placed on validation cases, which serve to establish confidence in the numerical tools and suction modeling approach. These include flat plate and airfoil configurations for which experimental and high-fidelity computational data are available. Demonstrating accurate prediction of transition onset and the influence of suction on boundary-layer development is critical to ensuring reliable optimization outcomes. Following validation, suction is applied upstream of the transition location to delay boundary-layer transition and reduce drag. Optimizations are performed for various suction velocities and suction region configurations. For infinite swept wings, suction is shown to suppress crossflow instabilities, reducing drag while maintaining lift. Preliminary results for finite wings with HLFC demonstrate favourable performance trends and support the extension of this methodology to three-dimensional configurations. The full paper will present detailed comparisons of suction profiles, transition locations, and aerodynamic performance across cases, establishing the capability of HLFC in high-speed, high-sweep applications.

I. Nomenclature

A	=	airfoil area
b	=	span
c	=	chord
C_D	=	coefficient of drag
C_L	=	coefficient of lift
C_Q	=	coefficient of suction
e	=	total energy per unit volume
j	=	mass flux
l	=	length of suction zone for a flat plate
$\dot{m}$	=	mass flow rate per unit area
M	=	Mach number
Q_{suc}	=	total volumetric flow rate through the surface
$\mathbf{Q}_{\text{target}}$	=	solution vector of the conservative flow variables at an individual node
Re	=	Reynolds number
v_{suc}	=	suction speed
v_{w}	=	normal component of velocity
V_∞	=	free-stream velocity
Λ	=	sweep angle

---

*PhD Candidate, University of Toronto Institute for Aerospace Studies, AIAA Student Member, justin.pascual@mail.utoronto.ca

[†]Distinguished Professor of Computational Aerodynamics and Sustainable Aviation, University of Toronto Institute for Aerospace Studies, AIAA Associate Fellow, david.zingg@utoronto.ca

μ_∞	=	free-stream dynamic viscosity
ρ	=	density
ρ_w	=	local density at the wall
ρ_∞	=	free-stream density
ξ	=	curvilinear coordinate

II. Introduction

The commercial aviation industry has experienced significant growth over the past few decades. Excluding the temporary decline in travel due to the COVID-19 pandemic, demand for safe and efficient air travel has increased by approximately 6% annually [1]. This growing demand has heightened environmental concerns, driving interest in the development of more efficient aircraft designs [1]. Aerodynamic shape optimization supports this effort by iteratively simulating and refining designs to improve specific performance metrics, offering a more systematic and effective alternative to traditional manual design iteration methods.

For a typical commercial aircraft, viscous drag contributes roughly 50% of the overall drag while operating at cruise conditions [2]. As flow passes over a surface, it transitions from laminar to turbulent, with turbulent flow having higher frictional forces and a thicker boundary layer, increasing the overall drag. To delay this transition from laminar to turbulent flow, flow control methods can be implemented to translate the transition location further downstream, increasing the region of laminar flow [3]. There are two main mechanisms through which flow transitions, the first being Tollmien-Schlichting (TS) instabilities, which occur in two-dimensional boundary layers in the form of vortices aligned in the spanwise direction. These instabilities are highly receptive to disturbances in the flow, and are amplified as they are advected downstream, resulting in the flow transition to turbulent [4]. The second mechanism is crossflow (CF) instabilities which arise on swept wings and are characterized by an inflection point in the transverse velocity profile. This inflection point causes the flow to be unstable, resulting in streamwise vortices that transition the flow to turbulence.

To improve aerodynamic efficiency by delaying the transition from laminar to turbulent flow, one promising passive technique is natural laminar flow (NLF), which relies on careful wing shaping to extend the laminar flow region. However, designing for NLF presents challenges due to competing requirements for suppressing different types of instabilities. For instance, favorable pressure gradients help delay Tollmien–Schlichting (TS) instabilities but tend to amplify crossflow (CF) instabilities. Additionally, while increasing the wing sweep angle reduces wave drag, it also intensifies CF instabilities, leading to higher viscous drag. These trade-offs involving conflicting pressure gradients and sweep angles result in NLF being limited to modest sweep angle and Reynolds number applications [5, 6].

At high sweep angles and Reynolds numbers, active laminar flow control techniques become necessary. Hybrid Laminar Flow Control (HLFC) addresses this by combining the passive shaping strategies of NLF with active boundary-layer suction. Together, shaping and suction modify the boundary-layer profiles to effectively delay the onset of transition. The best candidates for this technique are the wings and empennage because of their large wetted area and typically high sweep, with the nacelles and other surfaces still being considered for other drag reduction techniques [7].

The concept of using suction across the entirety of both the upper and lower surfaces of the wing was experimentally investigated by NACA in the Langley low-turbulence pressure tunnel [8]. This experiment used a NACA 64A010 airfoil with a sintered bronze surface to create very fine holes through which to apply suction. While operating at low speeds ($M \approx 0.3$) and low Reynolds number ($Re = 6 \times 10^6$) combinations, this experiment was able to demonstrate the capability of boundary-layer suction to laminarize the boundary layer. ~~Measurements taken at 83% of the chord show a much fuller, laminar profile compared to when suction is not used.~~

In another experiment, NASA explored the use of suction over the full upper and lower surfaces of a wing in the Langley Laminar-Flow-Control Experiment [9–12]. The study employed a supercritical airfoil in both unswept and swept configurations, aiming to validate transition prediction theories and compare the effectiveness of slotted versus perforated suction surfaces. This experiment considered temperature gradients and porosity in the calculation for suction efficiency. The results demonstrated that suction could successfully delay transition to as far back as 60% of the chord, confirming the ability of both suction surface types to move the transition location downstream.

Building on earlier experiments, Fisher and Fischer demonstrated the effectiveness and reliability of active laminar flow control on a JetStar aircraft during the Leading-Edge Flight Test (LEFT) [13]. The aircraft was equipped with both slotted suction and perforated suction surface configurations, and additional measures were tested to protect the suction system from insect, ice, and particulate contamination during takeoff; such as Krueger flaps with integrated deicer nozzles. Both configurations were successfully implemented, with the slotted suction proving more effective at delaying transition. The perforated surface, ~~however,~~ was prone to clogging from insect and dust due to its very small holes.

Computationally, Sudhi et al. combined active laminar flow control implementation with aerodynamic shape optimization for two-dimensional airfoils [14]. Using XFOIL, an aerodynamic solver coupled with an e^N transition prediction method, the transition location was determined. Drag-minimization optimizations were performed both with and without boundary-layer suction, with the onset of suction treated as a design variable to shape an optimal suction distribution. This optimized suction profile, applied upstream of the natural transition location, successfully delayed transition to 80% of the chord and yielded a 30% drag reduction relative to the no-suction optimized case. Expanding on this approach, Sudhi et al. further explored hybrid laminar flow control (HLFC) for transonic infinite swept wings operating at high Reynolds numbers, where crossflow instabilities dominate [15]. By simultaneously optimizing airfoil shape and suction distribution using a multi-objective genetic algorithm, they demonstrated that HLFC could apply to designs at higher sweep angles and Reynolds numbers. At a Reynolds number of 30×10^6 and sweep angle of 22.5°, HLFC configurations achieved up to 25% drag reduction over NLF designs, which outperformed fully turbulent designs by 27%.

The objective of the current work is to implement boundary-layer suction for both infinite swept and finite wing configurations under conditions representative of HLFC-equipped aircraft in cruise. The focus is on reducing overall drag through aerodynamic shaping and suction parameters, including suction velocity and distribution, while ensuring a net aerodynamic drag benefit. This work supports the development of efficient high-speed, high-sweep aircraft such as twin-aisle transports and blended wing-body configurations. To validate the suction boundary condition implementation, several benchmark cases; including flat plate flow, airfoil experiments, and high-speed swept-wing configurations.

Section III outlines the flow solver, transition prediction model, and aerodynamic shape optimization framework, including the modeling of active laminar flow control. Section IV presents the validation cases performed and results of lift-constrained drag minimization of two-dimensional airfoils with and without sweep and finite wings, incorporating suction in various ways. Finally, conclusions and future work are presented in Section V.

III. Methodology

Aerodynamic shape optimization is carried out using Jetstream, the high-fidelity optimization framework developed in-house at the University of Toronto Institute for Aerospace Studies. Jetstream comprises five core components: a Newton-Krylov-Schur flow solver for the Reynolds-Averaged Navier–Stokes (RANS) equations [16, 17]; a transition-prediction model based on empirical local correlations, coupled with the one-equation Spalart–Allmaras (SA) turbulence model [18, 19]; a unified geometry parameterization and mesh deformation scheme based on linear elasticity [20]; the SNOPT gradient-based optimizer used alongside a discrete-adjoint gradient method [21]; and a combination of free-form deformation (FFD) and axial deformation for geometry control [22]. The framework has been extended to support active boundary-layer suction through the implementation of a suction boundary condition.

A. RANS Flow Solver

The flow solver, Diablo [16, 17], is a multiblock, parallel, implicit solver that employs second-order summation-by-parts (SBP) operators for spatial discretization and uses simultaneous approximation terms (SATs) [23] to enforce boundary and block interface conditions. SATs act as penalty terms that drive the solution toward a specified target state at the boundaries. The SBP-SAT discretization of the governing equations results in a nonlinear system, which is solved using Newton's method in two distinct phases: an approximate-Newton phase followed by an inexact-Newton phase. In the first phase, an approximate Jacobian is used in conjunction with the implicit Euler method, with a gradual increase in time step. In the second phase, matrix-free matrix-vector products are used to approximate the exact Jacobian, enabling a more aggressive time step ramp-up. The transition between phases is triggered when the total residual decreases by five orders of magnitude. In both phases, the resulting linear systems are solved using the preconditioned Krylov iterative solver GMRES.

B. Transition Prediction Model

The flow solver incorporates boundary-layer transition prediction using the SA-sLM2015cc model developed by Piotrowski and Zingg [18, 19, 24]. This model builds on the $\gamma\text{-}Re_{\theta t}$ framework; an empirical, correlation-based approach introduced by Langtry and Menter [25] to model Tollmien–Schlichting (TS) and crossflow (CF) instabilities. The $\gamma\text{-}Re_{\theta t}$ model includes two transport equations: one for γ, the intermittency function, and another for $Re_{\theta t}$, the momentum-thickness Reynolds number. The SA-sLM2015 model couples this transition framework with the one-equation Spalart–Allmaras turbulence model [26], and replaces non-smooth functions in the original formulation

with smoothed alternatives to ensure a continuous and differentiable design space. Piotrowski and Zingg later enhanced the model by incorporating compressibility corrections for both TS and CF instabilities, leading to the current version, SA-sLM2015cc [27].

C. Geometry Parametrization, Mesh Deformation, Geometry Control

The optimization framework integrates geometry parameterization with mesh deformation, following the method developed by Hicken and Zingg [20]. Each computational grid block is linked to a B-spline volume, where the control points on the surface provide a low-dimensional representation of the original geometry. A mesh deformation technique based on linear elasticity transmits changes in the surface control points to the interior mesh through the control volume. Geometry manipulation is handled using a hybrid approach that combines free-form and axial deformation methods [22]. The free-form deformation (FFD) volumes are constructed using B-spline volumes, while the axial curves are represented by B-spline curves. The FFD control points govern section shape, chord, and twist, whereas the axial control curves manage sweep, span, and dihedral. The deformation of the axial control curves is not needed for the infinite swept wing cases considered in this paper, but is used for the finite wing optimization cases.

D. Gradient-Based Optimization

The optimization process is performed using SNOPT [21], a gradient-based algorithm that operates within a sequential quadratic programming (SQP) framework and is capable of handling both linear and nonlinear constraints. Gradient information is obtained through the discrete-adjoint method [28, 29].

E. Suction Boundary Condition

To simulate suction on the wing surface, the boundary is treated as a no-slip wall with a prescribed normal velocity directed into the surface. This is implemented by modifying the simultaneous approximation term (SAT) associated with the no-slip adiabatic wall condition. In particular, the momentum terms at the boundary are adjusted to account for the imposed suction velocity. The solution vector, $\mathbf{Q}_{\text{target}}$, modified for the suction boundary condition is defined as:

$$\mathbf{Q}_{\text{target}} = \begin{bmatrix} \rho \\ \dfrac{\frac{\partial \xi}{\partial x} \cdot v_{\text{suc}} \cdot \rho}{\sqrt{\left(\frac{\partial \xi}{\partial x}\right)^2 + \left(\frac{\partial \xi}{\partial y}\right)^2 + \left(\frac{\partial \xi}{\partial z}\right)^2}} \\ \dfrac{\frac{\partial \xi}{\partial y} \cdot v_{\text{suc}} \cdot \rho}{\sqrt{\left(\frac{\partial \xi}{\partial x}\right)^2 + \left(\frac{\partial \xi}{\partial y}\right)^2 + \left(\frac{\partial \xi}{\partial z}\right)^2}} \\ \dfrac{\frac{\partial \xi}{\partial z} \cdot v_{\text{suc}} \cdot \rho}{\sqrt{\left(\frac{\partial \xi}{\partial x}\right)^2 + \left(\frac{\partial \xi}{\partial y}\right)^2 + \left(\frac{\partial \xi}{\partial z}\right)^2}} \\ e \end{bmatrix}, \tag{1}$$

where v_{suc} is the user-defined suction speed parameter and ξ is the curvilinear coordinate direction normal to the surface.

The implementation of Equation 1 with the appropriate inviscid and viscous SATs to create a suction boundary condition is defined in [30].

Suction will be implemented using a specified suction speed, v_{suc}, as stated above, and will be analyzed and plotted across the surface using the suction coefficient, C_Q, which is defined as:

$$C_Q = \frac{\rho_w v_{\text{suc}}}{\rho_\infty V_\infty} \tag{2}$$

where ρ_w and ρ_∞ represent the local wall density and the free-stream velocity, respectively. Equation 2 further expanded

upon to include the suction being applied across the entire surface as:

$$C_Q = \frac{Q_{\text{suc}}}{V_\infty bc} \tag{3}$$

where Q_{suc} is the total flow rate through the surface, and b and c are the non-dimensionalized span and chord of the airfoil surface, respectively.

IV. Results

This section presents the validation ~~and application~~ of the developed suction boundary condition ~~and aerodynamic shape optimization framework~~. First, two validation cases are discussed: boundary-layer suction applied to a flat plate and to a NACA 64A010 airfoil, demonstrating agreement with both computational and experimental reference data. Following validation, the methodology is applied to aerodynamic optimization studies involving both infinite swept and finite wings. For infinite swept wings, suction is applied to optimized geometries and through discrete slot implementations. For finite wings, suction is applied using both fixed-chord and adaptively located distributions with respect to the transition front. Each study aims to quantify the aerodynamic performance improvements achievable through the integration of active laminar flow control into the design process.

A. Suction Boundary Condition Validation Cases

To validate the accuracy of the implemented suction boundary condition, a series of test cases were conducted, covering both computational and experimental references. These include a flat plate case based on DLR TAU-Code simulations, a subsonic wind tunnel experiment using a NACA 64A010 airfoil with distributed suction through a porous bronze surface, and a transonic NASA Langley experiment involving a swept supercritical airfoil with slotted and porous suction configurations. Together, these cases confirm the physical fidelity of the boundary condition and its suitability for use in more complex three-dimensional optimization problems.

1. Boundary-layer Suction Applied to a Flat Plate

Fehrs implemented a no-slip wall boundary condition using an effusion mass flux boundary condition in the DLR TAU-Code [31] and validated it analytically. The mass flux j is the mass flow $\dot{m}$ per unit area A defined as:

$$j = \frac{\dot{m}}{A} = \rho v_w$$

where v_w is the wall normal velocity that is set to a negative value to result in an inflow condition, equivalent to v_{suc} from Equation 1. The suction coefficient in Equation 3 can be modified for the infinite span flat plate case as:

$$C_Q = \frac{-1}{V_\infty l} \int_0^l v_w(x) dx$$

where l represents the length over which we are applying suction, assuming a porous surface completely covered with suction holes.

The operating conditions, including the suction coefficient and free stream velocity are outlined in Table 2. The results in Figure 1 show the velocity profiles with respect to the similarity variable η which is defined as:

$$\eta = y \sqrt{\frac{V_\infty}{2\nu x}}$$

The present computational results show excellent agreement with the reference data, validating the accuracy of the implemented suction boundary condition. The results demonstrate that the implementation was able to accurately reproduce the expected boundary-layer behaviour under suction, as seen in prior simulations.

Table 2   Inflow conditions for flat plate with boundary-layer suction

Case	C_Q	$V_\infty \ (m/s)$	$\rho_\infty \ (kg/m^3)$	$\mu_\infty \ (kg/m \cdot s)$
1	8.33×10^{-4}	40	1.2	1.814×10^{-5}
2	4.16×10^{-3}	40	1.2	1.814×10^{-5}
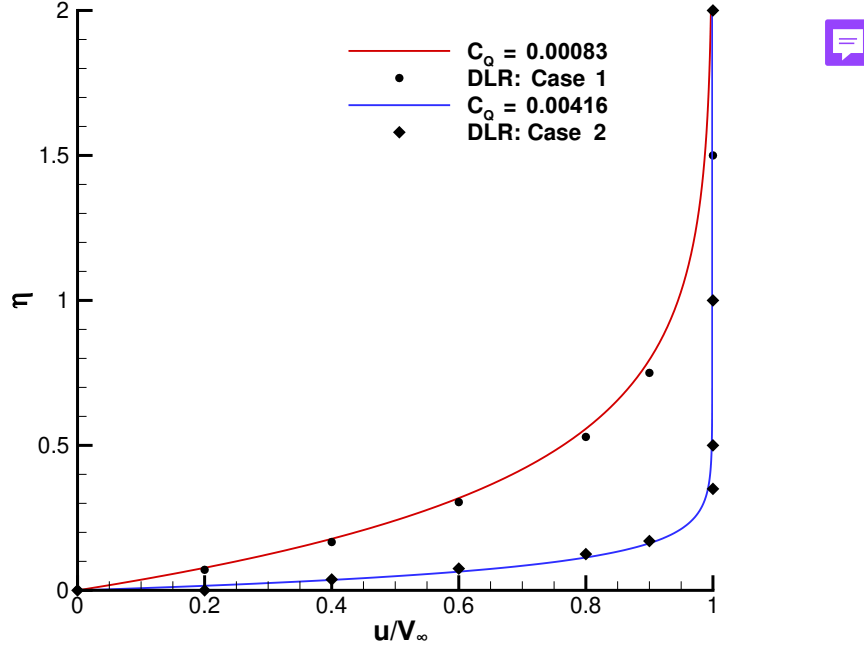
Fig. 1   Boundary-layer velocity profiles with two different suction coefficients produced using this work's suction boundary condition validated against DLR TAU-Code computational results (shown with symbols).

2. Boundary-layer Suction Applied to a NACA 64A010 Airfoil

Braslow et al. conducted experiments using a NACA 64A010 airfoil with a sintered bronze surface through which suction was applied [8]. Suction was applied across the entirety of the upper and lower surface, aside from a small portion at the leading edge. Figure 2 shows the approximate region over which suction was applied on the upper and lower surfaces at a suction coefficient of 0.0048. The wind tunnel was operated at a speed of $M \approx 0.3$ and $Re = 6 \times 10^6$ and the airfoil was fixed at $\alpha = 0°$.

The experiment captured the boundary-layer profiles at 83% of the chord and found that the flow was able to be sufficiently laminarized compared to when boundary-layer suction was not used. The computational mesh used for this validation case is a 270×182 O-grid. The results of this validation case are shown in Figure 3, with the computational results having an average error of approximately 5% when compared with the experimental results. ~~The computational model demonstrates slightly higher gradients in the near-wall region which would generate higher shear stresses compared to the experimental data, resulting in a slightly more conservative estimate of the effect of boundary-layer suction on drag reduction.~~

The full paper will also include a validation case from this experiment which investigated the effect of varying the applied suction coefficient on the transition location.
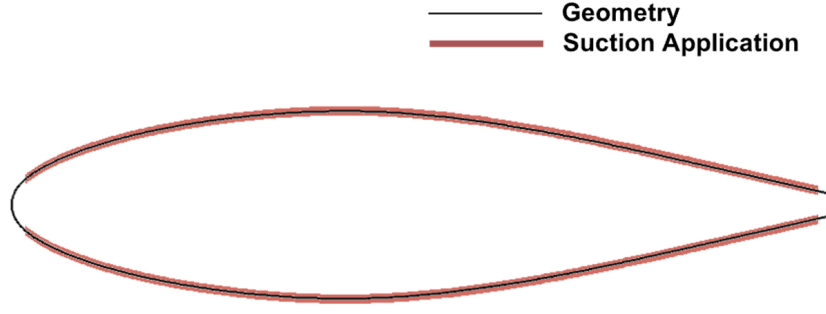
Fig. 2   Schematic demonstrating the approximate area over which suction was applied over the upper and lower surface through small sintered holes, excluding portions of the leading and trailing edge.
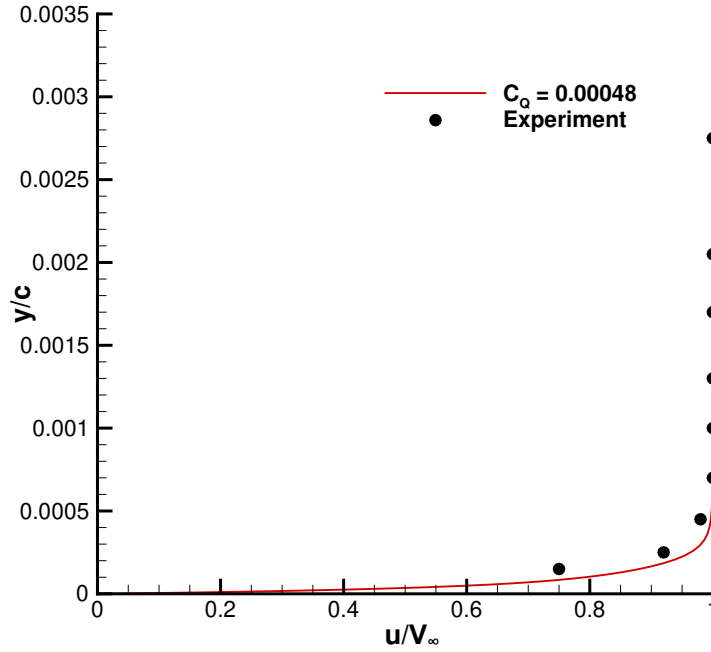
Fig. 3   Boundary-layer velocity profiles comparing this work's suction boundary condition against a NACA 64A010 wind tunnel experiment. The boundary-layer profiles are captured at 83% of the chord.

3. NASA Langley Laminar-Flow-Control Experiment

A swept, supercritical airfoil incorporating laminar-flow control was used for testing at transonic speeds [9–12]. The purpose of this research was to verify the theoretical drag reduction with the experimental data and to advance the application of analytical methods for the application of suction in slotted and porous configurations. Suction was applied across the entirety of the upper and lower surface of the wing for the porous configuration, and at specific locations for the slotted configuration. The operating conditions for this experiment consist of $M = 0.82$, $c = 7.07$ ft, $Re_c = 20 \times 10^6$, $C_L = 0.47$, $\Lambda = 23°$. A distribution plotting the suction coefficient, C_Q with respect to the chord describes the application of suction on the upper and lower surfaces. This study also considered temperature, porosity and permeability when determining the efficiency of the suction system, which will be investigated for the full paper. This study provides a relevant validation case for high-speed conditions representative of HLFC-capable aircraft at cruise conditions.

Following these validation cases, cases in the next section ~~will~~ apply the validated suction boundary condition to three-dimensional aerodynamic optimization problems. These include both infinite swept wing and finite wing configurations, where the goal is to evaluate the net benefit of suction, including power requirements.

B. Infinite Swept Wing Studies

The following cases were completed using the RAE2822 airfoil as the intial geometry. This geometry was then swept and operated at CRM-NLF conditions consisting of $M = 0.85$, $Re = 30 \times 10^6$, $C_L = 0.5$, $\Lambda = 35°$. The computational meshes used for this infinite swept wing are 475×243 O-grids. This geometry ~~also~~ has 21 axial free-form deformation curves for each surface.

1. Suction Application on an Optimized Natural Laminar Flow Geometry

Suction was applied at a fixed location on a geometry obtained from a lift-constrained drag minimization ~~study~~ without suction. A single-point optimization was performed at a target lift coefficient with a target lift coefficient of 0.50, subject to an area constraint and minimum thickness constraints. The optimization problem is summarized as:

$$
\begin{aligned}
\min_{\mathbf{X}} \quad & C_D(\mathbf{X}) \\
\text{s.t.} \quad & C_L = 0.50 \\
& A \geq A_{\text{init}} \\
& t/c \geq 0.15(t/c)_{\text{init}},
\end{aligned}
\tag{4}
$$

where $\mathbf{X}$ represents the design variable vector, C_L and C_D the lift and drag coefficients, respectively, and t/c the thickness-to-chord ratio for each FFD control point pair. The 'init' subscript indicates the value of the quantity from the baseline geometry. Previous results by Pascual and Zingg [30] investigated lower sweep angle and Reynolds number combinations. The present work shifts focus to conditions where aerodynamic shaping offers limited benefits due to CF instabilities, increasing reliance on active suction to delay transition and reduce drag. Since point optimizations with varying suction velocities will be included in the full paper.

2. Segmented Width Interval Suction Strategy (SWISS) Optimization Cases

To further investigate the effectiveness of suction for boundary-layer control, a Segmented Width Interval Suction Strategy (SWISS) was implemented. In this approach, suction is applied as a porous boundary condition over discrete spanwise intervals distributed across the full wing span with intervals every 5% and 10% of the chord, as shown in Figures 4a and 4b, respectively. Single-point optimizations will be performed with the same optimization problem as Equation 4 and will be included in the full paper. These cases will test the capability of the aerodynamic shape optimization framework to minimize drag using the given suction distribution, as well as provide vital information about the spatial effects of suction downstream.
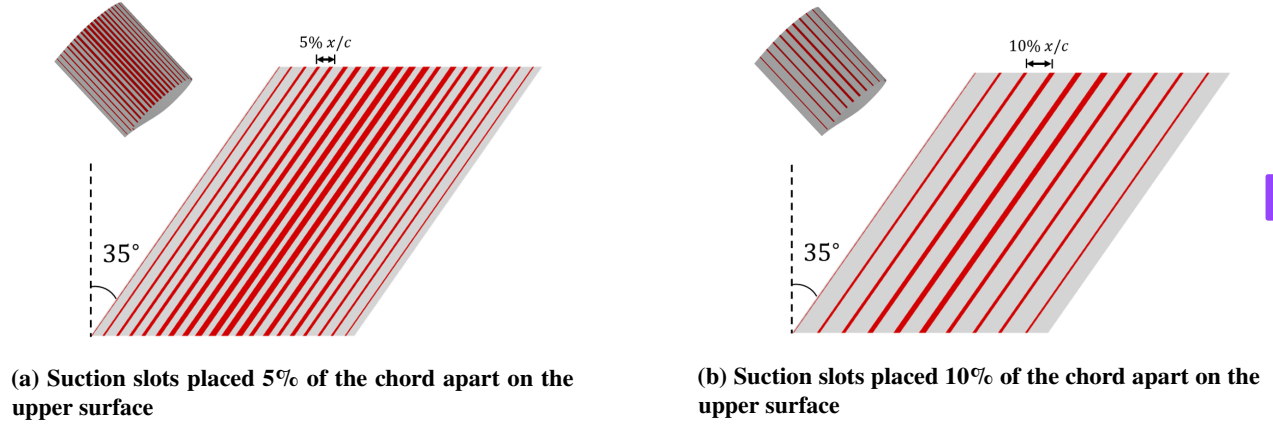
C. Finite Wing Studies

The following cases were completed using NLF-optimized results from Husain et al. [32] consisting of a wing with the RAE2822 airfoil section shape and a planform similar to the Airbus A320neo wing without winglets as the initial geometry. The wing has a half span of 59 feet, a mean aerodynamic chord of 14.4 feet, and a leading edge sweep angle of 28.36°. The geometry is embedded within an FFD volume with 9 FFD-volume cross-sections, each consisting of 11 FFD-volume control point pairs. The operating conditions consist of $M = 0.78$, $Re = 27 \times 10^6$ and $C_L = 0.5$. The FFD volume and control point pairs are illustrated in Figure 5 with the axial control points at the quarter-chord location.

1. Fixed Chord Suction Location

The transition front of the optimized geometry, shown in Figure 6a, was used to define a suction distribution positioned primarily upstream of the transition location. A single suction line was placed to remain just ahead of transition across as much of the span as possible. This distribution is illustrated in Figure 6b, where the red region indicates the suction location. A lift-constrained drag minimization study incorporating variations in suction speed,

(a) Suction slots placed 5% of the chord apart on the upper surface

(b) Suction slots placed 10% of the chord apart on the upper surface

Fig. 4 Suction is applied the prescribed distance apart along the chord starting at the leading edge. These schematics show suction applied only on the upper surface for clarity, ~~as the cases will have suction on the upper surface, the lower surface and both surfaces as well.~~ The suction slots are approximately 2.5% of the chord, and are enlarged in this schematic for clarity.
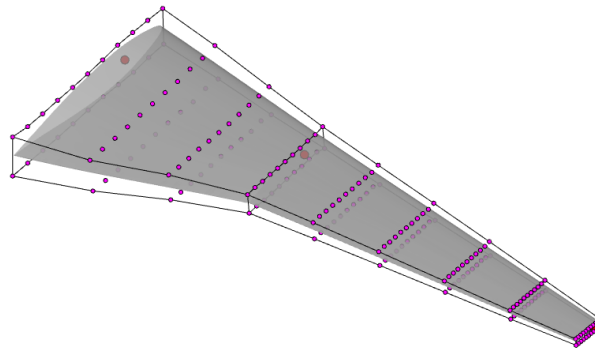
Fig. 5 Airbus A320neo axial (in red) and FFD (in magenta) control points

extent, and the number of suction zones, similar to the configurations in Section IV.B.2, will be presented in the full paper.

*2. Adaptive Suction Location With Respect to the Transition Front*

For this configuration, suction was applied upstream of the transition location shown in Figure 6b, at each spanwise node station, as illustrated schematically in Figure 7. This approach enables suction to act at a more appropriate location compared to the simpler method described in Section IV.C.1. The lift-constrained drag minimization ~~optimization~~ of this adaptive configuration will be included in the full paper.

V. Conclusions

This extended abstract presents an aerodynamic shape optimization framework that incorporates a validated boundary-layer suction implementation, applied to both infinite swept wings and finite wings. Initial results demonstrate that combining active suction with aerodynamic shaping can yield significant drag reductions. The suction boundary condition was carefully validated against experimental and computational benchmark cases to ensure its accuracy in predicting transitional flow behaviour and capturing the physics of active suction. The full paper will expand on this work by presenting several three-dimensional optimization studies on swept wings, comparing the net drag benefits of
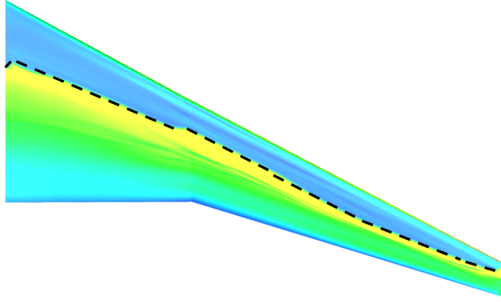
(a) Optimized geometry transition front
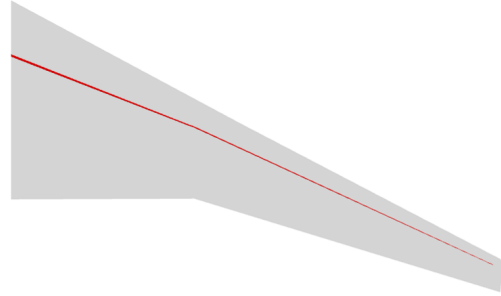
(b) Suction distribution applied to the upper surface

Fig. 6   Suction ~~was~~ applied as a single line primarily upstream of the average spanwise transition front, as shown in the optimized geometry. The suction region spans approximately 1% of the mean aerodynamic chord. A similar suction pattern was applied to the lower surface.
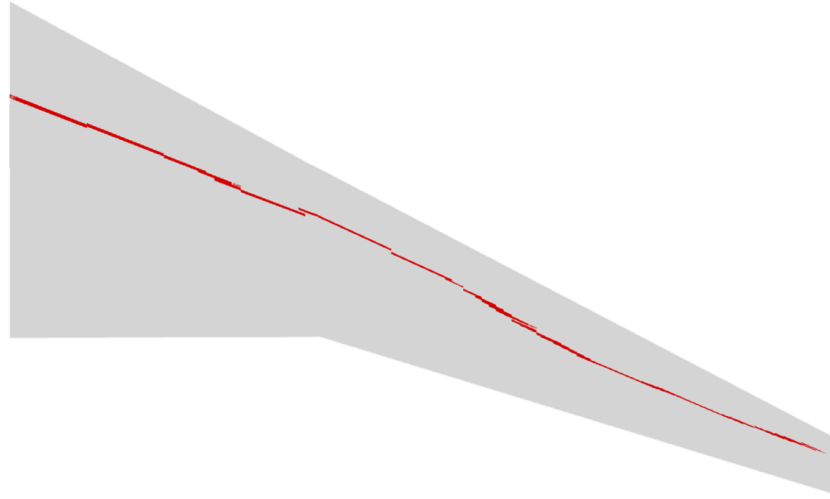
Fig. 7   Suction was ~~adaptively~~ placed based on spanwise transition location. Suction was applied at each spanwise station just upstream of the local transition point, covering approximately 1% of the mean aerodynamic chord. A similar approach was used for the lower surface.

suction with those achieved through natural laminar flow (NLF) across a range of sweep angles, Reynolds numbers, and suction configurations. Additionally, the impact of optimizing suction power consumption for improved net performance will be explored.

Acknowledgements

References

[1] Rashad, R., and Zingg, D. W., "Aerodynamic shape optimization for natural laminar flow using a discrete-adjoint approach," *AIAA J.*, Vol. 54, No. 11, 2016, pp. 3321–3337.

[2] Bushnell, D., "Overview of aircraft drag reduction technology," *AGARD Report 786*, 1992.

[3] Green, J. E., "Civil aviation and the environmental challenge," *The Aeronautical Journal*, Vol. 107, No. 1072, 2003, pp. 281–299. https://doi.org/10.1017/S0001924000013579.

[4] Green, J. E., "Civil aviation and the environment – the next frontier for the aerodynamicist," *The Aeronautical Journal*, Vol. 110, No. 1110, 2006, pp. 469–486. https://doi.org/10.1017/S0001924000001378.

[5] Lynde, M. N., and Campbell, R. L., "Computational Design and Analysis of a Transonic Natural Laminar Flow Wing for a Wind Tunnel Model," *35th AIAA Applied Aerodynamics Conference*, American Institute of Aeronautics and Astronautics, Denver, Colorado, 2017. https://doi.org/10.2514/6.2017-3058.

[6] Lynde, M. N., Campbell, R. L., Rivers, M. B., Viken, S. A., Chan, D. T., Watkins, A. N., and Goodliff, S. L., "Preliminary Results from an Experimental Assessment of a Natural Laminar Flow Design Method," *AIAA Scitech 2019 Forum*, American Institute of Aeronautics and Astronautics, San Diego, California, 2019. https://doi.org/10.2514/6.2019-2298.

[7] Johansen, J., and Sørensen, J. N., "Prediction of Laminar/Turbulent Transition in Airfoil Flows," *Journal of Aircraft*, Vol. 36, No. 4, 1999, pp. 731–734. https://doi.org/10.2514/2.2501.

[8] Braslow, A., Burrows, D., Tetervin, N., and Visconti, F., "Experimental and Theoretical Studies of Area Suction for the Control of the Laminar Boundary Layer on an NACA 64A010 Airfoil," Tech. Rep. Report 1025, NACA, 1951.

[9] Bobbitt, P. J., Ferris, J. C., Harvey, W. D., and Gordia, S. H., "Results for the Hybrid Laminar Flow Control Experiment," , No. NASA-TM-107582, 1992.

[10] Harvey, W. D., Harris, C. D., Brooks, C. W., Clukey, P. G., and Stack, J. P., "Design and Experimental Evaluation of a Swept, Supercritical LFC Airfoil," *Langley Symposium on Aerodynamics*, Vol. 1, 1986.

[11] Dagenhart, J. R., "Design of a Laminar-Flow-Control Supercritical Airfoil for a Swept Wing," *NASA, Langley Research Center, Hampton, VA, USA, CTOL Transport Technology*, 1978.

[12] Berry, S., Dagenhart, J. R., Brooks, C. W., and Harris, C. D., "Boundary-layer stability analysis of Langley Research Center 8-foot LFC experimental data," *NASA, Langley Research Center, Hampton, VA, USA, Research in Natural Laminar Flow and Laminar-Flow Control, Part 2*, 1987.

[13] Fisher, D. F., and Fischer, M. C., "Development flight tests of JetStar LFC leading-edge flight test experiment," *NASA, Langley Research Center, Research in Natural Laminar Flow and Laminar-Flow Control, Part 1*, 1987.

[14] Sudhi, A., Radespiel, R., and Badrya, C., "Design exploration of transonic airfoils for natural and hybrid laminar flow control applications," *J. Aircr.*, Vol. 60, No. 3, 2023, pp. 716–732.

[15] Sudhi, A., Radespiel, R., and Badrya, C., "Design exploration of transonic airfoils for natural and hybrid laminar flow control applications," *J. Aircr.*, Vol. 60, No. 3, 2023, pp. 716–732.

[16] Osusky, M., and Zingg, D. W., "A parallel Newton-Krylov-Schur flow solver for the Navier-Stokes equations discretized using summation-by-parts operators," *AIAA Journal*, Vol. 51, No. 12, 2008, pp. 2833–2851.

[17] Osusky, M., Hicken, J., and Zingg, D., "A Parallel Newton-Krylov-Schur Flow Solver for the Navier-Stokes Equations Using the SBP-SAT Approach," *48th AIAA Aerospace Sciences Meeting Including the New Horizons Forum and Aerospace Exposition*, American Institute of Aeronautics and Astronautics, Orlando, Florida, 2010. https://doi.org/10.2514/6.2010-116.

[18] Piotrowski, M., and Zingg, D. W., "Investigation of a Local Correlation-based Transition Model in a Newton-Krylov Algorithm," *AIAA Scitech 2019 Forum*, American Institute of Aeronautics and Astronautics, San Diego, California, 2019. https://doi.org/10.2514/6.2019-2299.

[19] Piotrowski, M. G. H., and Zingg, D. W., "Smooth Local Correlation-Based Transition Model for the Spalart–Allmaras Turbulence Model," *AIAA Journal*, Vol. 59, No. 2, 2021, pp. 474–492. https://doi.org/10.2514/1.J059784.

[20] Hicken, J. E., and Zingg, D. W., "Aerodynamic Optimization Algorithm with Integrated Geometry Parameterization and Mesh Movement," *AIAA Journal*, Vol. 48, No. 2, 2010, pp. 400–413. https://doi.org/10.2514/1.44033.

[21] Gill, P. E., Murray, W., and Saunders, M. A., "SNOPT: An SQP Algorithm for Large-Scale Constrained Optimization," *SIAM Journal on Optimization*, Vol. 12, No. 4, 2002, pp. 979–1006. https://doi.org/10.1137/S1052623499350013.

[22] Gagnon, H., and Zingg, D. W., "Two-Level Free-Form and Axial Deformation for Exploratory Aerodynamic Shape Optimization," *AIAA Journal*, Vol. 53, No. 7, 2015, pp. 2015–2026. https://doi.org/10.2514/1.J053575.

[23] Del Rey Fernández, D. C., Hicken, J. E., and Zingg, D. W., "Simultaneous Approximation Terms for Multi-dimensional Summation-by-Parts Operators," *Journal of Scientific Computing*, Vol. 75, No. 1, 2018, pp. 83–110. https://doi.org/10.1007/s10915-017-0523-7.

[24] Piotrowski, M. G., and Zingg, D. W., "Investigation of a Smooth Local Correlation-based Transition Model in a Discrete-Adjoint Aerodynamic Shape Optimization Algorithm," *AIAA SCITECH 2022 Forum*, American Institute of Aeronautics and Astronautics, San Diego, CA & Virtual, 2022. https://doi.org/10.2514/6.2022-1865.

[25] Langtry, R. B., and Menter, F. R., "Correlation-Based Transition Modeling for Unstructured Parallelized Computational Fluid Dynamics Codes," *AIAA Journal*, Vol. 47, No. 12, 2009, pp. 2894–2906. https://doi.org/10.2514/1.42362.

[26] Spalart, P. R., and Allmaras, S. R., "A one-equation turbulence model for aerodynamic flows," *La Recherche Aerospatiale*, , No. 1, 1994, pp. 5–21.

[27] Piotrowski, M., and Zingg, D., "Compressibility corrections to extend a smooth local correlation-based transition model to transonic flows," *The Aeronautical Journal*, Vol. 127, No. 1313, 2023, pp. 1141–1170. https://doi.org/10.1017/aer.2022.105.

[28] Jameson, A., Martinelli, L., and Pierce, N. A., "Optimum aerodynamic design using the Navier-stokes equations," *Theor. Comput. Fluid Dyn.*, Vol. 10, No. 1-4, 1998, pp. 213–237.

[29] Osusky, L., and Zingg, D., "A novel aerodynamic shape optimization approach for three-dimensional turbulent flows," *50th AIAA Aerospace Sciences Meeting including the New Horizons Forum and Aerospace Exposition*, American Institute of Aeronautics and Astronautics, Reston, Virigina, 2012.

[30] Pascual, J. M., and Zingg, D. W., "Progress in the application of an aerodynamic shape optimization capability using hybrid laminar flow control to airfoils and infinite swept wings," *AIAA SCITECH 2025 Forum*, American Institute of Aeronautics and Astronautics, Reston, Virginia, 2025.

[31] Fehrs, M., "Boundary layer suction modeling based on the DLR TAU-code effusion mass flux boundary condition," *Notes on Numerical Fluid Mechanics and Multidisciplinary Design*, Notes on numerical fluid mechanics and multidisciplinary design, Springer International Publishing, Cham, 2020, pp. 175–184.

[32] Husain, F., Simmons, I., and Zingg, D., "Application of aerodynamic shape optimization to swept natural laminar flow wings," *AIAA AVIATION FORUM AND ASCEND 2024*, American Institute of Aeronautics and Astronautics, Reston, Virginia, 2024.